Actinide Coordination Chemistry on Surfaces: Synthesis, Manipulation, and Properties of Thorium Bis(porphyrinato) Complexes

Erik Rheinfrank, Mathias Pörtner, Maria del Carmen Nuñez Beyerle, Felix Haag, Peter S Deimel, Francesco Allegretti, Knud Seufert, Johannes V Barth, Marie-Laure Bocquet, Peter Feulner, et al.

JACS
JOURNAL OF THE AMERICAN CHEMICAL SOCIETY
pubs.acs.org/JACS
Article

Actinide Coordination Chemistry on Surfaces: Synthesis, Manipulation, and Properties of Thorium Bis(porphyrinato) Complexes

Erik Rheinfrank, Mathias Pörtner, Maria del Carmen Nuñez Beyerle, Felix Haag, Peter S. Deimel, Francesco Allegretti, Knud Seufert, Johannes V. Barth, Marie-Laure Bocquet, Peter Feulner, and Willi Auwärter*

Cite This: https://doi.org/10.1021/jacs.1c04982
Read Online
ACCESS | Metrics & More | Article Recommendations | Supporting Information

ABSTRACT: Actinide-based metal−organic complexes and coordination architectures encompass intriguing properties and functionalities but are still largely unexplored on surfaces. We introduce the in situ synthesis of actinide tetrapyrrole complexes under ultrahigh-vacuum conditions, on both a metallic support and a 2D material. Specifically, exposure of a tetraphenylporphyrin (TPP) multilayer to an elemental beam of thorium followed by a temperature-programmed reaction and desorption of surplus molecules yields bis(porphyrinato)thorium ($Th(TPP)_2$) assemblies on Ag(111) and hexagonal boron nitride/Cu(111). A multimethod characterization including X-ray photoelectron spectroscopy, scanning tunneling microscopy, temperature-programmed desorption, and complementary density functional theory modeling provides insights into conformational and electronic properties. Supramolecular assemblies of $Th(TPP)_2$ as well as individual double-deckers are addressed with submolecular precision, e.g., demonstrating the reversible rotation of the top porphyrin in $Th(TPP)_2$ by molecular manipulation. Our findings thus demonstrate prospects for actinide-based functional nanoarchitectures.

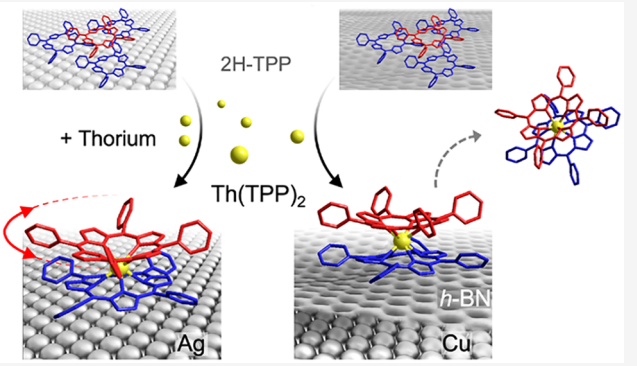

INTRODUCTION

Understanding the organometallic and coordination chemistry of actinide elements has drawn considerable interest in recent years.[1−8] High coordination numbers, a variety of available oxidation states, and the presence of 5f orbitals allow actinides to access reactivity modes and coordination environments that differ from the characteristics of d-block elements and lanthanides. As elemental metals, actinides are less homogeneous than their 4f counterparts. Their 5f electrons are localized exclusively for the late members of the series from Am through Lr. The early actinides through Pu show, in contrast to all lanthanides, itinerant 5f electrons that take part in bonding and screening, causing a parabolic dependence of the Wigner−Seitz radii on the atomic numbers similar to d-block elements, 5f density of states (DOS) directly at the Fermi edge seen in ultraviolet photoelectron spectroscopy (UPS), and well-screened inner-shell vacancies in X-ray photoelectron spectroscopy (XPS) (see ref 9 and references therein). These volatile 5f electrons enable oxidation states up to +7 for Np.[10] Comparing compounds with corresponding lanthanide and actinide atoms, bonds with actinide partners are generally considered to show increased covalent versus ionic character, whereas for the early group members Ce and Th, reversed results have been reported.[11,12] These properties, and the actinides' larger ionic radii that affect bond character and geometry, open prospects for novel functional materials, including single-molecule magnets[13−15] and coordination architectures, covering metal−organic coordination frameworks.[16−18] The latter structures are expected to play a relevant role in nuclear waste management.[19] Uranium- and thorium-based complexes and molecular materials have received the main attention, e.g., because of their interesting catalytic chemistry[20−24] and intriguing coordination structures reported.[6,17,18,25−32] Specifically, thorium tetrapyrrole complexes (including porphyrins, phthalocyanines, and corroles) were achieved,[6,33−35] affording double-decker bis(porphyrinato)thorium complexes, where a single thorium

Received: May 13, 2021

https://doi.org/10.1021/jacs.1c04982
J. Am. Chem. Soc. XXXX, XXX, XXX−XXX

center is sandwiched between two macrocyclic ligands.[36−38] In addition, the large half-lives of ^{232}Th (1.4×10^{10} years) and ^{238}U (4.47×10^{9} years) minimize radiation hazards compared to other, more short-lived actinides.

So far, most of this work on metal−organic actinide complexes has been carried out in solution or solid state. Single-molecule characterization, supramolecular assembly, and chemistry directly on surfaces remain unexplored—in stark contrast to the lanthanide counterparts (see below)—mainly because of safety restrictions due to radiation. Metal surfaces, however, provide excellent platforms to assemble and synthesize metal−organic complexes and functional molecular architectures and to control and monitor the structural, electronic, and magnetic properties under ultrahigh-vacuum (UHV) conditions.[39−42] Moreover, two-dimensional materials and ultrathin films can be used to reduce molecule−metal interactions that can adversely affect or mask intrinsic molecular properties, with a monolayer of insulating hexagonal boron nitride (*h*-BN) being a prominent example of such a decoupling layer.[43,44] Indeed, surface science experiments and complementary theoretical modeling have provided exciting insights into lanthanide-based tetrapyrrole complexes and coordination architectures on model surfaces,[45] with pioneering studies on double-decker and multidecker structures,[46−52] including $TbPc_2$ as an exemplary single-ion molecular magnet.[53−56] Thin decoupling layers were applied to improve the stability of the magnetic properties[51,55] or to manipulate the charge state of lanthanide−tetrapyrrole double-deckers.[50] As a downside, the intact deposition of such complexes by sublimation in a UHV environment poses severe challenges, with thermally induced molecular fragmentation or modifications often interfering with clean, homogeneous adsorbate structures,[46,52,57] even though molecular functionalization can favor successful deposition.[49] In situ synthesis of lanthanide tetrapyrrole double-deckers and multideckers was resorted to as a remedy and alternative, e.g., yielding $Ce(TPP)_2$, $Ce_2(TPP)_3$,[58] $Gd_{x-1}Pc_x$ (x = 1−5),[59] $TbPc_2$, and $Tb(tbu\text{-}Pc)_2$[60] complexes directly on noble metal supports.

Here, we introduce the in situ synthesis of $Th(TPP)_2$ (see Figure 1a−c) in a solvent-free UHV environment on two distinctly different substrates, namely, Ag(111) and *h*-BN/Cu(111). Our work thus expands on-surface metalation protocols, which are well-established for 3d metals,[61,62] alkali metals,[63] nonmetals,[64,65] and lanthanides,[58−60,66] to the actinide series. Along with extending tetrapyrrole surface science,[67,68] this study provides a rare example of a successful reaction on *h*-BN.[69−74]

The in situ synthesis process, inspired by the pioneering studies on lanthanide metalation,[45,58−60] is schematically illustrated in Figure 1d and e. It encompasses three steps: (1) growth of a precursor multilayer of 2H-TPP molecules on the substrate of choice; (2) deposition of elemental Th at room temperature (rt); and (3) thermal annealing at 500 K for several minutes to desorb unreacted multilayer components. The *h*-BN monolayer is prepared by chemical vapor deposition prior to the deposition of the molecules.[75] As sketched in the bottom panels of Figure 1d and e, the emerging surface morphologies are different for the two supports (Ag(111), Figure 1d; *h*-BN/Cu(111), Figure 1e). Furthermore, *h*-BN enables desorption and detection of the reaction products. The resulting $Th(TPP)_2$ sandwich complexes were investigated using X-ray photoelectron spectroscopy (XPS), scanning tunneling microscopy (STM), scanning tunneling spectroscopy (STS), and temperature-programmed desorption (TPD). On both supports, regular $Th(TPP)_2$ arrays are observed without a discernible difference in packing and molecular appearance. However, the electronic structure represented in dI/dV spectra reveals distinct differences, e.g., featuring a larger apparent electronic gap on *h*-BN/Cu(111). The twist angles between the two macrocyclic ligands were determined for $Th(TPP)_2$/Ag(111) and hint to a deviation from a perfect square antiprismatic coordination of the Th center. Complementary density functional theory (DFT) modeling reveals details of the molecular conformation, e.g., demonstrating an inverted dome shape of the upper TPP. Molecular manipulation applied to individual $Th(TPP)_2$ units anchored in a 2H-TPP layer induced the reversible rotation of the top porphyrin, thus demonstrating basic properties of a molecular rotational switch.[76] To this end, the large size of the Th center (ionic radius exceeding, e.g., the one of Tb)[77] might be instrumental in providing well-distanced macrocycles.

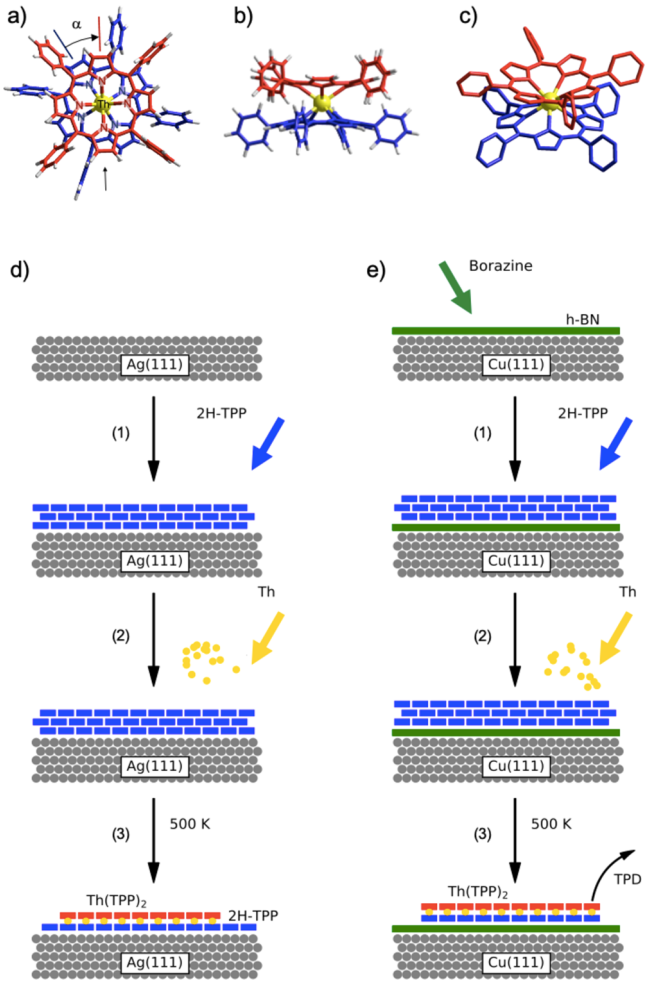

Figure 1. (a−c) DFT-optimized structure of a bis(porphyrinato)-thorium double-decker complex ($Th(TPP)_2$) in vacuum. The two TPP units connected via the Th center (yellow) are colored in red and blue, respectively. (a) Top view. α denotes the twist angle between the two macrocycles. (b) Side view (in the direction of the arrow in panel a). (c) 3D view (hydrogens omitted for clarity). (d, e) Schematic of the three-step synthesis route (1−3) for the formation of $Th(TPP)_2$ on Ag(111) (d) and *h*-BN/Cu(111) (e). See text for details.

https://doi.org/10.1021/jacs.1c04982
J. Am. Chem. Soc. XXXX, XXX, XXX−XXX

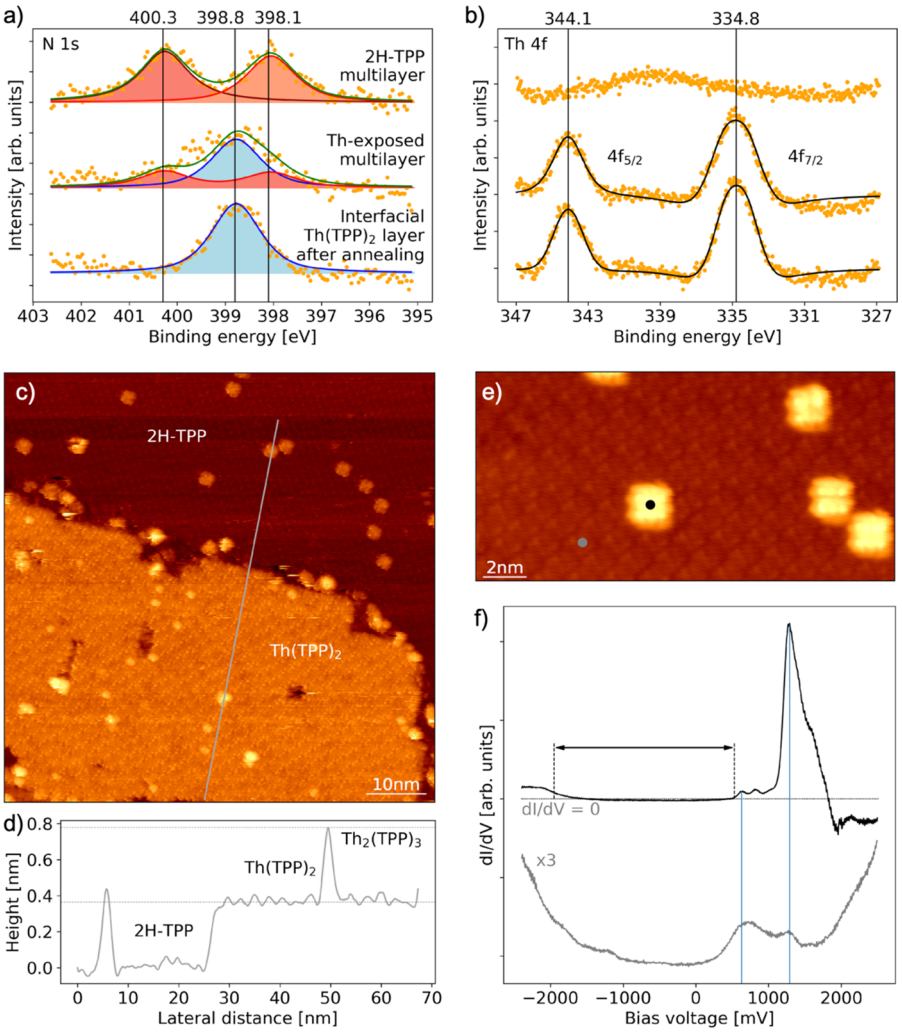

Figure 2. (a) Series of N 1s XP spectra representing a 2H-TPP multilayer on Ag(111) (top panel), the multilayer exposed to Th at rt (middle panel), and the resulting interfacial layer after thermal desorption of unreacted multilayer species (bottom panel). For each spectrum, fits are included for the individual components (see text for discussion). The respective binding energies are marked by the vertical lines with the values specified in eV. The maximum intensities of the spectra are normalized for better comparability. (b) Series of spin−orbit split Th 4f spectra representing the three synthesis steps described in panel a. (c) STM image of a $Th(TPP)_2$ island in a 2H-TPP array embedding individual $Th(TPP)_2$ units. (d) Apparent height profile along the path marked by the gray line in panel c. (e) Close-up STM image of individual $Th(TPP)_2$ in the 2H-TPP layer. The colored dots represent positions where dI/dV spectra were recorded (see panel f). (f) (Top panel) Characteristic dI/dV spectrum of $Th(TPP)_2$ revealing a large gap (marked by the arrow) and pronounced spectral features (see text for discussion). (Bottom panel) dI/dV reference spectrum of 2H-TPP. Tip stabilized at I_t = 60 pA and V_b = 2.5 V. Scanning conditions: (c) I_t = 0.7 nA, V_b = 1.7 V; (d) I_t = 0.7 nA, V_b = 1.7 V.

RESULTS AND DISCUSSION

Thorium Bis(porphyrinato) Complexes on Ag(111). The formation of $Th(TPP)_2$ complexes on Ag(111) was monitored by XPS, following each step of the synthesis process. The corresponding N 1s and Th 4f signatures including fits are shown in parts a and b of Figure 2, respectively. The evolution of the N 1s core-level spectrum clearly reflected the metalation of the TPP. Before the deposition of Th (Figure 2a, top panel), two separate peaks arose from the two inequivalent nitrogen atoms in 2H-TPP, i.e., the pyrrolic (−NH−) and iminic (−C═N−) species.[78] The binding energies (E_b = 400.3 and 398.1 eV) matched the reported values for 2H-TPP multilayers on Ag(111) (400.2 and 398.1 eV).[79] After dosing Th, the N 1s signature changed considerably (Figure 2a, middle panel), reflecting a superposition of signals from unreacted 2H-TPP and a new species tentatively assigned to Th-metalated TPP. Following annealing to 500 K, the width of the spectral feature was clearly reduced, and the signal could be described by a main peak at E_b = 398.8 eV (Figure 2a, bottom panel). This indicates the desorption of unreacted TPP multilayer components and a dominating contribution of metalated TPP, where all four nitrogen atoms in the macrocycle are chemically equivalent. Such behavior is well-known from the in situ metalation of tetrapyrroles[61,62,78] and consistent with the formation of $Th(TPP)_2$ complexes. The resulting N 1s binding energy compares well with values reported for Fe-TPP (398.7 eV[79] and 398.4 eV[80]), Ti-TPP (398.6 eV[81]), Ru-TPP (398.6 eV[82]), and Co-TPP (398.8 eV[78]) on Ag(111). However, it is considerably larger than the N 1s binding energy (398.1 eV) attributed to the N−Tb component in $TbPc_2$ double-deckers on Ag(111).[60] Figure 2b depicts the Th $4f_{7/2}$ and $4f_{5/2}$ core levels that exhibit strong spin−orbit splitting. The binding energies (see Figure 2b) match the ones reported for oxidized Th (ThO_2, E_b = 344.2

https://doi.org/10.1021/jacs.1c04982
J. Am. Chem. Soc. XXXX, XXX, XXX−XXX

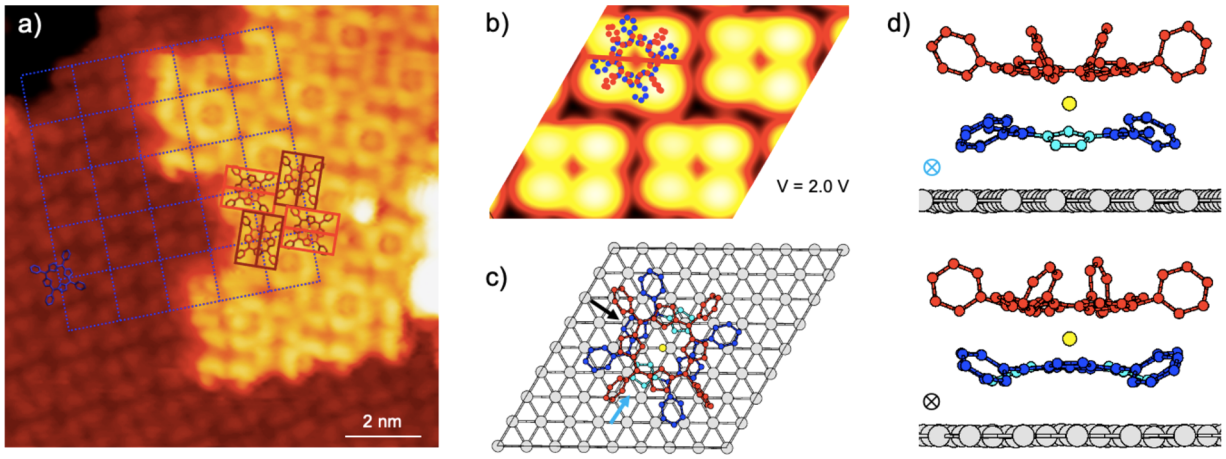

Figure 3. (a) STM image of a $Th(TPP)_2$ island embedded in a 2H-TPP array revealing submolecular contrast. The $Th(TPP)_2$ centers are in registry with the surrounding dense-packed 2H-TPP lattice (blue grid). The orientations of the upper porphyrin in adjacent $Th(TPP)_2$ units differ by ~90°, as indicated by the molecular models framed in two shades of red. The main axis of the top ligand is marked by a line. A comparison to 2H-TPP (blue model) reveals a rotation of the upper porphyrin in $Th(TPP)_2$ by (33 ± 6)° or (−56 ± 6)° with respect to the bottom one. Scanning conditions: I_t = 0.1 nA, V_b = 2.0 V. (b) STM image simulation based on the DFT-optimized structure of $Th(TPP)_2/Ag(111)$ (see panels c and d) computed at 2 V bias voltage. (c, d) Structural model with top ligand, bottom ligand, Th center, and Ag surface colored in red, blue, yellow, and light gray, respectively. (c) Top view. The κ-pyrroles are highlighted in turquoise. (d) Side views in the two directions indicated by the colored arrows in panel c. Hydrogens are omitted for clarity.

and 334.9 eV) rather than the ones of the pure metal species (E_b = 342.4 and 333.1 eV).[83] This finding shows that the Th is incorporated into the porphyrin's macrocycle and consistent with a Th oxidation state +IV, as expected for $Th(TPP)_2$ complexes.[35]

Because the XPS experiments point to a successful synthesis of $Th(TPP)_2$, STM measurements were performed to get insight into the surface morphology of the resulting system. Figure 2c shows an STM image recorded after applying the synthesis procedure described earlier using a low Th dose. The silver surface was completely covered by well-ordered molecular arrays. The top part was identified as a 2H-TPP monolayer. The bottom part featured a compact island with an apparent height exceeding the surrounding 2H-TPP film. Because only a homogeneous monolayer and no second layer species were observed after annealing the 2H-TPP multilayer without the addition of Th,[58] this island was assigned to $Th(TPP)_2$. Both the 2H-TPP layer and the $Th(TPP)_2$ array hosted individual units of larger apparent height that were scattered across the surface. The data showed no indication of Th-modified single-decker species.[66] Taking a height profile along the gray line revealed that the individual species embedded in the 2H-TPP monolayer and the compact $Th(TPP)_2$ island exhibited the same apparent height (see Figure 2d). Accordingly, the former were assigned to $Th(TPP)_2$ units. The coexistence of compact $Th(TPP)_2$ arrays and individual $Th(TPP)_2$ units was reminiscent to the situation of in situ synthesized $Ce(TPP)_2$[58] and $Gd(Pc)_2$[59] on Ag(111). Similar to other tetrapyrrole double-decker complexes,[52,59] the apparent height of $Th(TPP)_2$ was strongly bias-dependent because it reflected the electronic structure of the complex (see below). Accordingly, a meaningful comparison of apparent heights of chemically different $M(TPP)_2$ units was not straightforward. It is noted that the apparent height of $M(TPP)_2$ increased with increasing positive sample bias voltage until a height value was reached that stayed roughly constant with further moderate increase of the bias. When considering the apparent height at bias voltages where this "plateau" was reached (1.9 V for $Th(TPP)_2$, 2.4 V for $Ce(TPP)_2$), the values for $Th(TPP)_2$ (0.34 nm) and $Ce(TPP)_2$ (0.33 nm)[58] measured relative to the surrounding 2H-TPP layer compared well. Given the similar covalent[84] and ionic radii[77] of Th and Ce, this finding was not surprising. Because of their apparent height of 0.78 nm (with regard to 2H-TPP), the additional bright species within the $Th(TPP)_2$ island were tentatively assigned to $Th_2(TPP)_3$ triple-decker species.

The electronic properties of $Th(TPP)_2/Ag(111)$ were explored by STS. Figure 2f represents a typical dI/dV spectrum taken above the center of an individual $Th(TPP)_2$ double-decker (see black marker in Figure 2e), showing well-defined features. The unoccupied spectral region (V_b > 0 V) was dominated by a distinct peak at 1290 mV trailed by a shoulder and a negative differential resistance (NDR) region. At ~670 mV a faint double protrusion was observed. Because its lower-energy peak (onset at ~540 mV) was the first unoccupied feature detected, it was associated with the lowest unoccupied molecular orbital (LUMO). The occupied spectral region (V_b < 0 V) revealed an onset at approximately −1950 mV, which was tentatively assigned to the highest occupied molecular orbital (HOMO). Consequently, the apparent HOMO−LUMO gap amounted to ~2490 mV. Within an experimental accuracy of ±30 mV (i.e., given by the lateral and vertical positions of the tip), the spectra recorded on several $Th(TPP)_2$ units provided consistent values for the characteristic spectral features. While their assignment to distinct molecular orbitals was not straightforward, some conclusions could be drawn from the spectra. The low conductivity around the Fermi level (E_F, V_b = 0 V) and the corresponding emergence of an electronic gap, as well as the NDR signature, indicated a weak interaction of the probed molecular states with the metallic support. Reference spectra recorded on 2H-TPP (gray marker in Figure 2e) did not show a gap but rather broad resonances. Interestingly, the onset of the prominent feature in the unoccupied range that was previously assigned to the LUMO

https://doi.org/10.1021/jacs.1c04982
J. Am. Chem. Soc. XXXX, XXX, XXX−XXX

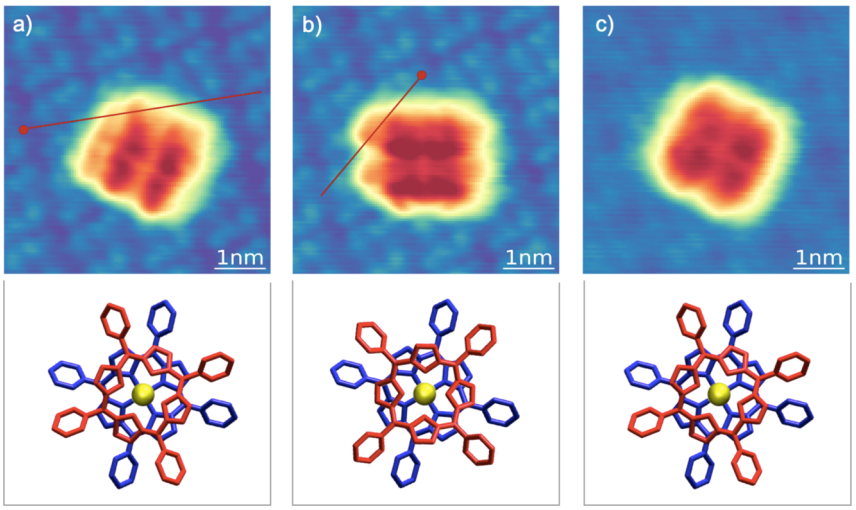

Figure 4. Reversible tip-induced mechanical rotation of the top porphyrin in individual $Th(TPP)_2$ units. (Top row) STM images of a double-decker embedded in a 2H-TPP array. (Bottom row) Corresponding structural models (top view). (a) Initial configuration. By laterally moving the tip from the position marked by the red dot along the red line, a rotation of the top porphyrin is induced. (b) $Th(TPP)_2$ after this first manipulation step. The red line marks the subsequently applied manipulation path. (c) In this second manipulation step, the $Th(TPP)_2$ returned to its initial configuration. The apparent change in resolution is related to a minor modification of the STM tip apex. Lateral manipulation parameters: I_t = 3.5 nA, V_b = 0.05 V. Scanning parameters: I_t = 0.11 nA, V_b = 1.7 V.

of 2H-TPP[66,85] coincided with the onset of the LUMO of $Th(TPP)_2$.

On a more general note, the overall spectral shape including the features described wearlier for $Th(TPP)_2$ was reflected in several different bis(tetrapyrrole)lanthanoid systems on Ag(111) and Cu(111),[47,57] even if the energies of the features depended on the specific center atom, the tetrapyrroles, and the substrate involved. Nonetheless, as far as we know, a conclusive interpretation of these features is lacking in the literature to date. The apparent HOMO−LUMO gap of $Th(TPP)_2$/Ag(111) exceeded the ones of $Ce(TPP)_2$/Ag(111) (~2160 mV)[47] and CePcTPP/Ag(111) (~1550 mV).[57] Whereas the latter case highlighted the influence of the Pc ligand in the heteroleptic complex, the two homoleptic TPP systems revealed the influence of the central atom.

In a next step, we aimed for a detailed insight into the self-assembled $Th(TPP)_2$ arrays and shed some light on the conformation of the double-deckers. Figure 3 a shows an STM image of a $Th(TPP)_2$ island embedded in a 2H-TPP array featuring intramolecular resolution. At a bias voltage of V_b = 2.0 V, the 2H-TPPs showed a square-like shape with four protrusions and a central depression, as previously reported.[86] The $Th(TPP)_2$, on the other hand, featured a more rectangular shape with four extended protrusions, peripheral lobes, and a central depression. Because of the apparent 2-fold symmetry of the double-decker at this specific bias voltage, we defined a main symmetry axis along the dark central line crossing the $Th(TPP)_2$ (see Figure 3a). A model overlay of the top porphyrin showed that this main axis represented the N−Th−N directions and indicated that the phenyl ring orientations as well as a nonplanar macrocycle distortion contributed to the 2-fold appearance. Importantly, two distinct orientations of the porphyrin top ligand of $Th(TPP)_2$ were observed, differing by ~90° (see dark and light-red rectangular outlines in Figure 3a). In the molecular array, the orientation alternated from molecule to molecule. The centers of $Th(TPP)_2$ were placed on positions in the registry with the surrounding 2H-TPP lattice with a nearest-neighbor distance of 1.39 nm (see blue grid in Figure 3a), implying that the $Th(TPP)_2$'s bottom ligands followed the packing of the 2H-TPPs. On the basis of this assumption, one could determine the twist angle α between the bottom and top macrocycles of $Th(TPP)_2$, which amounted to (33 ± 6)° for the dark-red species. This value matched the twist angle of ~30° reported for crystalline $Th(TPP)_2$ and indicated deviations from a square, anti-prismatic coordination geometry.[37] For the bright-red species, α = (−56 ± 6)° (with "−" signaling counterclockwise rotation), reflecting the same macrocycle registry if a 4-fold symmetry of the macrocycle was assumed. Additionally, $Th(TPP)_2$ featuring the opposite chirality, i.e., twist angles of (−33 ± 6)° or (56 ± 6)°, occurred in islands with identical packing. The same twist angles were found for individual double-deckers embedded in 2H-TPP, which signaled that packing effects did not play a dominant role. The conformation of $Th(TPP)_2$ thus differed from that of $Ce(TPP)_2$, where twist angles of (15 ± 5)° and (45 ± 5)° were reported for individual and dense-packed double-deckers, respectively.[58] Nonetheless, the packing scheme featuring alternating orientations of top ligands differing by 90° was reminiscent of self-assembled $Ce(TPP)_2$ islands on Ag(111).[58]

A more detailed insight into the structure of $Th(TPP)_2$ adsorbed on Ag(111) was provided by DFT (Figure 3b−d and Figure S1 in the Supporting Information). The calculations revealed that the top and bottom ligands displayed different geometries. The bottom porphyrin, coupled to the metallic substrate, exhibited a saddle conformation and a moderate tilt of the peripheral phenyl groups (dihedral angles ~40°). The top ligand adopted an inverted dome shape and a larger tilt of the phenyl rings (dihedral angles from 64° to 86°, average = 74°). From the superposition of the STM image simulation and the double-decker structure (see Figure 3b), one could see that the STM contrast was entirely governed by the four phenyl rings of the top ligand. The quantitative agreement between STM simulations and experiments indeed allowed one to assign the dark central line (characteristic of the $Th(TPP)_2$ appearance at 2 V) to a N−Th−N axis, with the 2-

https://doi.org/10.1021/jacs.1c04982
J. Am. Chem. Soc. XXXX, XXX, XXX−XXX

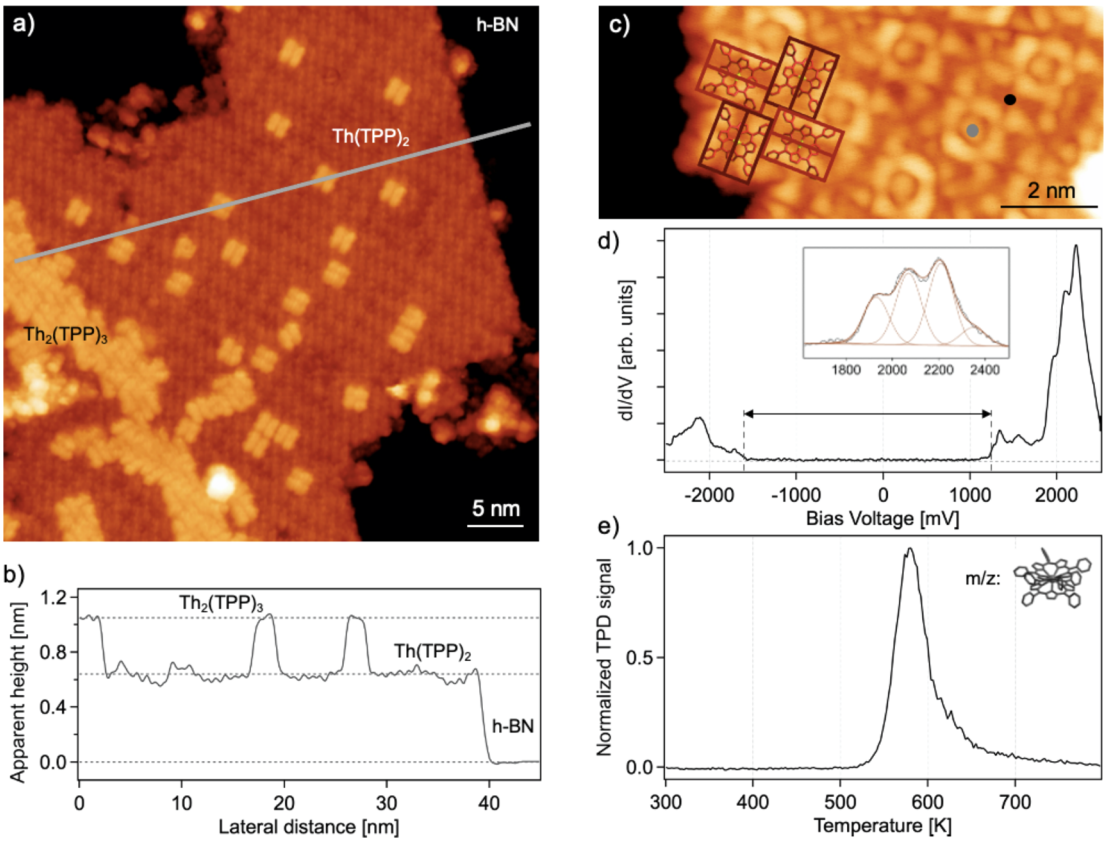

Figure 5. (a) STM image of a self-assembled $Th(TPP)_2$ island on *h*-BN/Cu(111). Third-layer species within the island are tentatively attributed to $Th_2(TPP)_3$. (b) Height profile along the line highlighted in panel a. (c) STM image of a $Th(TPP)_2$ island revealing the same packing as on Ag(111). Two orientations of top porphyrins rotated by ~90° with respect to each other are observed, as highlighted by the superimposed rectangles and models (compare to Figure 3a). (d) dI/dV spectrum of $Th(TPP)_2$ (averaged from three individual spectra) recorded above the center of the molecule (see black marker in panel c). The arrow marks the apparent gap. The inset shows a magnification of the substructure of the main peak (recorded above the position represented by the gray marker in panel c) after subtracting a polynomial background. The signal is fitted by four Gaussians with fixed separation and fixed width. Tip stabilized at I_t = 100 pA, V_b = 2.0 V, z-approach = 0.5 Å. (e) TPD spectrum of the relevant mass-to-charge ratio m/z, showing the desorption of $Th(TPP)_2$ around 580 K. Scanning parameters: (a) I_t = 0.8 nA, V_b = 1.725 V; (c) I_t = 0.5 nA, V_b = 2.0 V.

fold symmetry induced by the phenyl groups tilted in opposite directions (see Figure 3b–d). Interestingly, DFT yielded a higher stability (by 60 meV) for a $Th(TPP)_2$ configuration with a twist angle α = 30° than for the one with α = 45°, thus confirming the experimental observation (which seems counterintuitive when only considering steric repulsion). Additional structural information (such as Th–N bond lengths and $Th(TPP)_2$ adsorption heights) extracted from the DFT optimization is provided in Figure S1, including a comparison of $Th(TPP)_2$ on Ag(111), Cu(111), and *h*-BN. It is noted that the inverted dome shape observed for the top decker might promote distinct interactions with nonplanar guest species, such as fullerenes.[47]

Next, we experimentally addressed the structural stability of $Th(TPP)_2$ and demonstrated the rotatability of the upper porphyrin by applying an STM-based molecular manipulation procedure. First, an STM image with scanning parameters not affecting the $Th(TPP)_2$ was taken. Then, the STM tip approached the surface and laterally moved across the periphery of the upper porphyrin of the double-decker to exert a torque, keeping the current constant. Subsequently, the tip was retracted, and another STM image with the original parameters was taken to check whether the manipulation was successful. Figure 4 shows the reversible azimuthal rotation of the top ligand of a $Th(TPP)_2$ anchored in the 2H-TPP network by applying said procedure. Starting from the position marked by a red dot, the STM tip was moved along the red path, rotating the upper TPP out of its equilibrium orientation. From the initial configuration in Figure 4a, an apparent clockwise rotation of ~70° led to the configuration in Figure 4b. Using the same manipulation procedure but a different tip path, the process caould be reversed, as shown by the apparent counterclockwise rotation from panel b to panel c of Figure 4, after which the molecule was again in its initial state. During the whole procedure, the top porphyrin remained in registry with the unaffected 2H-TPP network. The two distinct configurations (Figure 4a and b) reflected the twist angles as discussed earlier. These lateral manipulation experiments were performed successfully on several molecules. In some cases, the removal of the complete $Th(TPP)_2$ occurred, exposing a bare Ag(111) patch.[52] Apparently, the interaction between the Th center and the upper porphyrin macrocycle was sufficiently strong to prevent decomposition of $Th(TPP)_2$ upon interaction with the STM tip under the applied manipulation parameters. This experiment also showed that the vertical separation of the two TPP units by the Th center was large enough to allow reversible rotational switching of the upper porphyrin, even though details of the process (such as the

https://doi.org/10.1021/jacs.1c04982
J. Am. Chem. Soc. XXXX, XXX, XXX–XXX

sense of rotation) remained elusive to the STM methodology. Nonetheless, STM measurements of this system carried out at rt showed a rectangular outline of the individual molecules as in the low-temperature imaging (not shown), indicating that the rotation barrier was high enough to inhibit thermally induced rotation on the time scale of the STM imaging, even at rt. Indeed, a DFT-calculated energy profile between two configurations revealed a considerable energy barrier with a transition state featuring aligned phenyl moieties of upper and lower porphyrin ligands (see Figure S2). In summary, we concluded that surface-anchored $Th(TPP)_2$ represented a molecular rotor switchable by an external stimulus, in agreement with findings for surface-confined lanthanide tetrapyrrole sandwich compounds.[58,87,88]

Thorium Bis(porphyrinato) Complexes on *h*-BN/Cu(111). After demonstrating the successful assembly of $Th(TPP)_2$ double-decker complexes on the Ag(111) surface, we now discuss the results of applying the same synthesis protocol to the *h*-BN/Cu(111) support (see Figure 1e), again yielding the targeted $Th(TPP)_2$ complexes. The *h*-BN spacer layer was introduced to access intrinsic molecular properties, reducing potentially detrimental effects on electronic and magnetic characteristics caused by interaction with a metallic support.[50,51,55] Figure 5a shows an STM image of the resulting surface structure. Dense-packed islands of $Th(TPP)_2$ embedding individual, as well as aggregated, third-layer molecules were observed. However, no surrounding 2H-TPP layer remained on the surface. This allowed for determination of the apparent height of the complexes relative to the bare *h*-BN support. The line profile in Figure 5b reveals an apparent height of 0.64 nm (at V_b = 1.725 V) for the island assigned to $Th(TPP)_2$ and of 1.05 nm for the third-layer species.

Submolecularly resolved STM images exhibited the same order of the $Th(TPP)_2$ islands as on Ag(111) (Figure 5c). Specifically, a 2-fold appearance of $Th(TPP)_2$ was observed at V_b = 2 V, and every second upper TPP ligand was rotated by ~90° with respect to its neighbors, as reflected by the framed dark- and light-red models superimposed on the STM image in Figure 5c. Because no 2H-TPP was left as a "marker" for the orientation of the bottom TPP, the twist angle of $Th(TPP)_2$/*h*-BN/Cu(111) remained elusive in our experiment. DFT modeling (Figure S1) revealed a similar conformation for $Th(TPP)_2$ on Ag(111) and *h*-BN, with a larger adsorption height on the latter support.

The absence of 2H-TPP after annealing the Th-exposed 2H-TPP multilayer at 500 K showed that unreacted 2H-TPP readily desorbed from *h*-BN/Cu(111) at this temperature, whereas $Th(TPP)_2$ only efficiently desorbed at higher temperature (see below). Indeed, the desorption of a somewhat smaller tetrapyrrole (2H-porphine) from *h*-BN/Cu(111) occurred at 470 K.[89]

A characteristic STS signature of a $Th(TPP)_2$ complex on *h*-BN/Cu(111) is shown in Figure 5d. Even though the key features already discussed for the d*I*/d*V* spectrum of $Th(TPP)_2$/Ag(111) remained clearly discernible, the spectrum on $Th(TPP)_2$/*h*-BN showed distinct modifications. The dominant resonance in the unoccupied spectral region appeared at ~2000 mV and showed a pronounced substructure with a series of peaks separated by an average spacing of (142 ± 5) mV (see inset in Figure 5d). A faint feature with an onset at ~1240 mV was assigned to the LUMO, following the notation introduced earlier for $Th(TPP)_2$/Ag(111). The occupied spectral feature comprised a subtle increase in conductivity at approximately −1650 mV, the HOMO, followed by a peak at −2130 mV. Accordingly, the apparent HOMO−LUMO gap (2890 mV) of $Th(TPP)_2$/*h*-BN/Cu(111) was noticeably increased by ~400 mV compared to $Th(TPP)_2$ adsorbed on Ag(111), pointing to an efficient electronic decoupling of $Th(TPP)_2$ from the Cu(111) by the *h*-BN spacer. Indeed, the substructure of the main resonance was reminiscent of vibronic excitations, as reported for phthalocyanines on *h*-BN/Ir(111) and *h*-BN/Rh(111).[90,91] However, both the intensity sequence and the peak separation were distinct. The measured energy spacing (142 mV, 1145 cm^{-1}) and the rescaled energy spacing, considering the voltage drop across the *h*-BN layer[91] (118 mV, 952 cm^{-1}), fell in a range of different vibrational modes reported for $Th(TPP)_2$.[38] It should be noted that the energy of $Th(TPP)_2$'s spectral features could vary with lateral position due to the corrugated electronic landscape provided by the *h*-BN/Cu(111) support.[92]

To corroborate the in situ formation of $Th(TPP)_2$ complexes and to study the corresponding desorption characteristics, a qualitative TPD characterization was carried out. A $Th(TPP)_2$/*h*-BN/Cu(111) sample was prepared by the procedure described earlier and subsequently annealed with a linear heating rate (1 K/s), recording the signal that corresponded to the mass-to-charge ratio of the thorium porphyrinato double-decker (1456 amu). Specifically, due to the limited resolution at such a high mass, we integrated over a small mass range (1456 ± 10 amu). A typical desorption spectrum is depicted in Figure 5e, revealing a maximum at a temperature of ~580 K. The TPD experiment thus provided two important messages. (1) The detection of the $Th(TPP)_2$ proved the successful in situ synthesis of bis(porphyrinato) thorium on *h*-BN/Cu(111), complementing the STM data. (2) The *h*-BN support afforded the thermal desorption of intact, interfacial tetrapyrrole adsorbates and reaction products that could subsequently be characterized, e.g., by mass spectrometry, complementing TPD results on porphyrin multilayers and films.[63,64]

CONCLUSIONS

We introduced actinides for interfacial coordination chemistry. Specifically, we reported the fabrication of homoleptic thorium bis(porphyrinato) complexes, namely, $Th(TPP)_2$, on well-defined model surfaces under UHV conditions. The N 1s and Th 4f XPS data revealed the bonding of the Th center to the TPP macrocycles. Submolecular resolution in STM imaging combined with complementary DFT modeling gave insight into the conformation of $Th(TPP)_2$, characterized by distinct twist angles between bottom and top porphyrin ligands (33° and 56°), an inverted dome shape of the latter, and tilted terminal phenyl moieties. The twist angles deviated from the ones reported for its lanthanide counterpart, $Ce(TPP)_2$ on Ag(111), reflecting the character of the actinide center. The self-assembled $Th(TPP)_2$ arrays on Ag(111) and *h*-BN/Cu(111) showed the same packing, with alternating orientations of the top ligands differing by 90°, consistent with reports on the $Ce(TPP)_2$ islands. The reversible rotation of the top porphyrin by tip manipulation demonstrated the potential of actinide-based tetrapyrrole double-deckers for molecular switching and machinery, with the large size of the Th ion facilitating rotational dynamics by separation of the two macrocycles. From a different perspective, this study showed for the first time the formation of a supramolecular double-

https://doi.org/10.1021/jacs.1c04982
J. Am. Chem. Soc. XXXX, XXX, XXX−XXX

decker complex on a two-dimensional material, namely, monolayer *h*-BN, and demonstrated the benefits of such a decoupling layer. Specifically, the *h*-BN support permitted the thermal desorption of intact double-decker units, corroborating the successful in situ $Th(TPP)_2$ synthesis, and allowed one to observe details of the double-deckers's electronic structure including vibronic signatures by STS. Thus, no metal surface was needed as a catalyst for this multistep synthesis of actinide-based metal−organic complexes.

We anticipate that the reported synthesis protocol is generally applicable to diverse tetrapyrrole derivatives, additional actinide elements, and other supports (including two-dimensional materials), thus opening pathways to actinide complexes and nanostructures with tailored properties and functionalities. Accordingly, surface-confined actinide-based metal−organic complexes and supramolecular architectures might perfectly complement lanthanide-based systems for potential application in molecular magnetism, quantum technologies, sensing, and heterogeneous catalysis.

EXPERIMENTAL SECTION

Experimental Setup and Data Processing. XPS measurements were conducted in a custom-built UHV chamber incorporating a XPS system with a lab-based X-ray source and a hemispherical electron analyzer from SPECS (Phoibos 100). All data were acquired using a Mg anode (1253.6 eV) with a pass energy of 10 eV in normal emission. During the acquisition of the XP spectra, the base pressure was $<1 \times 10^{-9}$ mbar and the sample was kept at rt. The spectra were calibrated against the binding energy of the Ag $3d_{5/2}$ core level. Pseudo-Voigt functions were used to fit the spectra. The background in the Th 4f spectra was corrected by subtracting a Shirley background following the method of Herrera-Gomez et al.[93] For the N 1s spectra, the background subtraction was performed by fitting the clean Ag(111) signal with a polynomial function and subtracting this adjusted curve from the data.

STM measurements were carried out in a separate custom-built UHV system housing a commercial low-temperature CreaTec STM operating at 7 K with a base pressure of $<3 \times 10^{-10}$ mbar. All images were recorded in constant-current mode using a chemically etched W tip.

The TPD experiments were performed in a custom-designed UHV chamber with a base pressure of low 10^{-10} mbar, which could be lowered to 6×10^{-11} mbar during the TPD acquisition by employing liquid nitrogen cooled traps. A K-type junction, which was in direct contact with the Cu(111) crystal, was used to measure the temperature of the sample. The quadrupole mass spectrometer (QMS) used in the TPD experiments was a Balzers QMA 160 rod system enclosed within a copper cap,[94] in front of which the Cu(111) crystal was positioned as close as 1 mm. A mass range up to 3000 amu was covered with 400 kHz Extrel electronics. The temperature was varied linearly, exploiting radiative heating from a glowing W filament placed behind the sample and using a purpose-built PID controller (Schlichting Physikalische Instrumente HS 130). The experimental chamber also contained XPS equipment (a dual-anode X-ray source and a SPECS Phoibos 100 hemispherical electron analyzer with 2D-CCD detector) for optimization of the preparation procedures and consistency checks. STM data were processed using Gwyddion,[95] python3, and the WSxM software (www.wsxm.es). A Gaussian filter was applied to Figure 3a.

Sample Preparation. The Ag(111) and Cu(111) single crystals were cleaned by repeated cycles of Ar^+ or Ne^+ sputtering at an energy of 800−1000 eV and annealing to ∼730 K (silver) and ∼830 K (copper) for several minutes. The 2H-TPP molecules (Sigma-Aldrich, ≥99% purity) were evaporated via organic molecular beam epitaxy (OMBE) from a quartz crucible that was resistively heated to $T_{evap} \approx$ 260 °C, while the sample was kept at rt. Th atoms were deposited from a home-built water-cooled evaporator with integrated temperature-stabilized quartz microbalance. Our source was a 0.2 mm Th wire (Goodfellow, 99.5% purity) wrapped by multiple windings (0.5 mm pitch) of a 0.1 mm W wire onto a 0.3 mm W support wire. The whole assembly was resistively heated, and the evaporation rate was measured with the microbalance; see ref 96 for details. The *h*-BN monolayer was grown by chemical vapor deposition of borazine ($B_3N_3H_6$, Katchem, Czech Republic), following a published recipe.[75]

Theoretical Methodology. DFT calculations were carried out using the Vienna Ab Initio Simulation Package (VASP)[97] with the Perdew−Burke−Ernzerhof (PBE) exchange correlation.[98] The projector-augmented wave potential with a cutoff energy of 400 eV was used to describe the electron−ion interaction.[99] We considered the metallic lattice parameter a_{Ag} = 4.07 Å (corresponding to a Ag−Ag distance of 2.878 Å). Hence, we used the GGA PBE-D3 method[100] to achieve structural and electronic convergence of the large supercells at Gamma point. The simulated STM images were carried out by applying the Tersoff and Hamann theory in a plane-wave basis set as implemented in the STMpw code.[101] To visualize the simulations, we used Crystal Maker 10 software (www.crystalmaker.com).

ASSOCIATED CONTENT

Supporting Information

The Supporting Information is available free of charge at https://pubs.acs.org/doi/10.1021/jacs.1c04982.

Additional structural information from DFT calculations, including coordinates of $Th(TPP)_2$ (PDF)

AUTHOR INFORMATION

Corresponding Author

Willi Auwärter − *Physics Department E20, Technical University of Munich, D-85748 Garching, Germany;* orcid.org/0000-0001-9452-4662; Email: wau@tum.de

Authors

Erik Rheinfrank − *Physics Department E20, Technical University of Munich, D-85748 Garching, Germany*

Mathias Pörtner − *Physics Department E20, Technical University of Munich, D-85748 Garching, Germany*

Maria del Carmen Nuñez Beyerle − *Physics Department E20, Technical University of Munich, D-85748 Garching, Germany*

Felix Haag − *Physics Department E20, Technical University of Munich, D-85748 Garching, Germany*

Peter S. Deimel − *Physics Department E20, Technical University of Munich, D-85748 Garching, Germany*

Francesco Allegretti − *Physics Department E20, Technical University of Munich, D-85748 Garching, Germany;* orcid.org/0000-0001-6141-7166

Knud Seufert − *Physics Department E20, Technical University of Munich, D-85748 Garching, Germany;* orcid.org/0000-0002-4111-0965

Johannes V. Barth − *Physics Department E20, Technical University of Munich, D-85748 Garching, Germany;* orcid.org/0000-0002-6270-2150

Marie-Laure Bocquet − *PASTEUR, Département de Chimie, Ecole Normale Supérieure, PSL University, Sorbonne Université, CNRS, F-75005 Paris, France;* orcid.org/0000-0001-7122-4907

Peter Feulner − *Physics Department E20, Technical University of Munich, D-85748 Garching, Germany*

Complete contact information is available at: https://pubs.acs.org/10.1021/jacs.1c04982

https://doi.org/10.1021/jacs.1c04982
J. Am. Chem. Soc. XXXX, XXX, XXX−XXX

Notes

The authors declare no competing financial interest.

■ ACKNOWLEDGMENTS

We thank Nicolas Lorente for fruitful discussions. This work was supported by the European Research Council Consolidator Grant NanoSurfs (no. 615233), the ANR-DFG project RidePorph, and the Deutsche Forschungsgemeinschaft (DFG) via the Cluster of Excellence e-conversion. M.-L.B. acknowledges granted access to the French HPC resources of TGCC and CINES under Grant A7-A0070807364 by GENCI. F.H., F.A., and J.V.B. are grateful for funding from the TUM International Graduate School of Science and Engineering (IGSSE) via the DFG, GSC 81. W.A. acknowledges funding by the DFG via a Heisenberg professorship.

■ REFERENCES

(1) Arnold, P. L.; Casely, I. J. F-Block N-Heterocyclic Carbene Complexes. *Chem. Rev.* **2009**, *109*, 3599−3611.

(2) Albrecht-Schmitt, T. E. Actinide Materials Adopt Curvature: Nanotubules and Nanospheres. *Angew. Chem., Int. Ed.* **2005**, *44*, 4836−4838.

(3) Jones, M. B.; Gaunt, A. J. Recent Developments in Synthesis and Structural Chemistry of Nonaqueous Actinide Complexes. *Chem. Rev.* **2013**, *113*, 1137−1198.

(4) Edelmann, F. T.; Farnaby, J. H.; Jaroschik, F.; Wilson, B. Lanthanides and actinides: Annual survey of their organometallic chemistry covering the year 2018. *Coord. Chem. Rev.* **2019**, *398*, 113005.

(5) Neidig, M. L.; Clark, D. L.; Martin, R. L. Covalency in f-element complexes. *Coord. Chem. Rev.* **2013**, *257*, 394−406.

(6) Ward, A. L.; Buckley, H. L.; Lukens, W. W.; Arnold, J. Synthesis and Characterization of Thorium(IV) and Uranium(IV) Corrole Complexes. *J. Am. Chem. Soc.* **2013**, *135*, 13965−13971.

(7) Klamm, B. E.; Windorff, C. J.; Celis-Barros, C.; Marsh, M. L.; Meeker, D. S.; Albrecht-Schmitt, T. E. Experimental and Theoretical Comparison of Transition-Metal and Actinide Tetravalent Schiff Base Coordination Complexes. *Inorg. Chem.* **2018**, *57*, 15389−15398.

(8) Walter, O. Actinide Organometallic Complexes with π-Ligands. *Chem. - Eur. J.* **2019**, *25*, 2927−2934.

(9) Moore, K. T.; van der Laan, G. Nature of the 5*f* states in actinide metals. *Rev. Mod. Phys.* **2009**, *81*, 235−298.

(10) Gibson, J. K. Gas-phase chemistry of actinide ions: probing the distinctive character of the 5f elements. *Int. J. Mass Spectrom.* **2002**, *214*, 1−21.

(11) Cheisson, T.; Kersey, K. D.; Mahieu, N.; McSkimming, A.; Gau, M. R.; Carroll, P. J.; Schelter, E. J. Multiple Bonding in Lanthanides and Actinides: Direct Comparison of Covalency in Thorium(IV)- and Cerium(IV)-Imido Complexes. *J. Am. Chem. Soc.* **2019**, *141*, 9185−9190.

(12) Berryman, V. E. J.; Whalley, Z. J.; Shephard, J. J.; Ochiai, T.; Price, A. N.; Arnold, P. L.; Parsons, S.; Kaltsoyannis, N. Computational analysis of M-O covalency in M(OC6H5)4 (M = Ti, Zr, Hf, Ce, Th, U). *Dalton Trans.* **2019**, *48*, 2939−2947.

(13) Rinehart, J. D.; Harris, T. D.; Kozimor, S. A.; Bartlett, B. M.; Long, J. R. Magnetic Exchange Coupling in Actinide-Containing Molecules. *Inorg. Chem.* **2009**, *48*, 3382−3395.

(14) Rinehart, J. D.; Long, J. R. Exploiting single-ion anisotropy in the design of f-element single-molecule magnets. *Chem. Sci.* **2011**, *2*, 2078−2085.

(15) Layfield, R. A. Organometallic Single-Molecule Magnets. *Organometallics* **2014**, *33*, 1084−1099.

(16) Ok, K. M.; Sung, J.; Hu, G.; Jacobs, R. M. J.; O'Hare, D. TOF-2: ALarge 1D Channel Thorium Organic Framework. *J. Am. Chem. Soc.* **2008**, *130*, 3762−3763.

(17) Li, Y.; Weng, Z.; Wang, Y.; Chen, L.; Sheng, D.; Diwu, J.; Chai, Z.; Albrecht-Schmitt, T. E.; Wang, S. Surprising coordination for low-valent actinides resembling uranyl(vi) in thorium(iv) organic hybrid layered and framework structures based on a graphene-like (6,3) sheet topology. *Dalton Trans.* **2016**, *45*, 918−921.

(18) Dolgopolova, E. A.; Rice, A. M.; Shustova, N. B. Actinide-based MOFs: a middle ground in solution and solid-state structural motifs. *Chem. Commun.* **2018**, *54*, 6472−6483.

(19) Dolgopolova, E. A.; Ejegbavwo, O. A.; Martin, C. R.; Smith, M. D.; Setyawan, W.; Karakalos, S. G.; Henager, C. H.; zur Loye, H.-C.; Shustova, N. B. Multifaceted Modularity: A Key for Stepwise Building of Hierarchical Complexity in Actinide Metal-Organic Frameworks. *J. Am. Chem. Soc.* **2017**, *139*, 16852−16861.

(20) Arnold, P. L.; Ochiai, T.; Lam, F. Y. T.; Kelly, R. P.; Seymour, M. L.; Maron, L. Metallacyclic actinide catalysts for dinitrogen conversion to ammonia and secondary amines. *Nat. Chem.* **2020**, *12*, 654−659.

(21) Andrea, T.; Eisen, M. S. Recent advances in organothorium and organouranium catalysis. *Chem. Soc. Rev.* **2008**, *37*, 550−567.

(22) Fox, A. R.; Bart, S. C.; Meyer, K.; Cummins, C. C. Towards uranium catalysts. *Nature* **2008**, *455*, 341−349.

(23) Ephritikhine, M. The vitality of uranium molecular chemistry at the dawn of the XXIst century. *Dalton Trans.* **2006**, 2501−2516.

(24) Jantunen, K. C.; Scott, B. L.; Kiplinger, J. L. A comparative study of the reactivity of Zr(IV), Hf(IV) and Th(IV) metallocene complexes: Thorium is not a Group IV metal after all. *J. Alloys Compd.* **2007**, *444*−*445*, 363−368.

(25) Girolami, G. S.; Milam, S. N.; Suslick, K. S. Synthesis and characterization of actinide mono and bis porphyrin complexes. *Inorg. Chem.* **1987**, *26*, 343−344.

(26) Sessler, J. L.; Seidel, D.; Vivian, A. E.; Lynch, V.; Scott, B. L.; Keogh, D. W. Hexaphyrin(1.0.1.0.0.0): An Expanded Porphyrin Ligand for the Actinide Cations Uranyl (UO22+) and Neptunyl (NpO2+). *Angew. Chem., Int. Ed.* **2001**, *40*, 591−594.

(27) Sessler, J. L.; Gorden, A. E.; Seidel, D.; Hannah, S.; Lynch, V.; Gordon, P. L.; Donohoe, R. J.; Tait, C. D.; Keogh, D. W. Characterization of the interactions between neptunyl and plutonyl cations and expanded porphyrins. *Inorg. Chim. Acta* **2002**, *341*, 54−70.

(28) Krivovichev, S. V.; Kahlenberg, V.; Kaindl, R.; Mersdorf, E.; Tananaev, I. G.; Myasoedov, B. F. Nanoscale Tubules in Uranyl Selenates. *Angew. Chem., Int. Ed.* **2005**, *44*, 1134−1136.

(29) Tutson, C. D.; Gorden, A. E. Thorium coordination: A comprehensive review based on coordination number. *Coord. Chem. Rev.* **2017**, *333*, 27−43.

(30) Wang, Y.; Liu, W.; Bai, Z.; Zheng, T.; Silver, M. A.; Li, Y.; Wang, Y.; Wang, X.; Diwu, J.; Chai, Z.; Wang, S. Employing an Unsaturated Th4+ Site in a Porous Thorium-Organic Framework for Kr/Xe Uptake and Separation. *Angew. Chem., Int. Ed.* **2018**, *57*, 5783−5787.

(31) Li, P.; Wang, X.; Otake, K.-i.; Lyu, J.; Hanna, S. L.; Islamoglu, T.; Farha, O. K. Synthetic Control of Thorium Polyoxo-Clusters in Metal-Organic Frameworks toward New Thorium-Based Materials. *ACS Appl. Nano Mater.* **2019**, *2*, 2260−2265.

(32) Bell, N. L.; Maron, L.; Arnold, P. L. Thorium Mono- and Bis(imido) Complexes Made by Reprotonation of cyclo-Metalated Amides. *J. Am. Chem. Soc.* **2015**, *137*, 10492−10495.

(33) Lux, F.; Dempf, D.; Graw, D. Diphthalocyaninato-thorium(IV) and -uranium(IV). *Angew. Chem., Int. Ed. Engl.* **1968**, *7*, 819−820.

(34) Martarano, L. A.; Wong, C.-P.; Horrocks, W. D.; Ponte-Goncalves, A. M. Luminescence of yttrium(III), lutetium(III), and thorium(IV) porphyrin complexes. *J. Phys. Chem.* **1976**, *80*, 2389−2393.

(35) Dormond, A.; Belkalem, B.; Charpin, P.; Lance, M.; Vigner, D.; Folcher, G.; Guilard, R. Thorium and uranium porphyrins. Synthesis and crystal structure of bis(acetylacetonato)(2,3,7,8,12,13,17,18-octaethylporphyrinato)thorium(IV). *Inorg. Chem.* **1986**, *25*, 4785−4790.

(36) Kadish, K. M.; Moninot, G.; Hu, Y.; Dubois, D.; Ibnlfassi, A.; Barbe, J. M.; Guilard, R. Double-decker actinide porphyrins and phthalocyanines. Synthesis and spectroscopic characterization of

https://doi.org/10.1021/jacs.1c04982
J. Am. Chem. Soc. XXXX, XXX, XXX−XXX

neutral, oxidized, and reduced homo- and heteroleptic complexes. *J. Am. Chem. Soc.* **1993**, *115*, 8153−8166.
(37) Girolami, G. S.; Gorlin, P. A.; Milam, S. N.; Suslick, K. S.; Wilson, S. R. Bis(porphyrin)actinide complexes and their radical cations and dications. *J. Coord. Chem.* **1994**, *32*, 173−212.
(38) Lomova, T. N.; Berezin, B. D. Porphyrin Complexes with p, d, and fMetals in High Oxidation States: Structures, Electronic Absorption, and IR Spectra. *Russ. J. Coord. Chem.* **2001**, *27*, 85−104.
(39) Barth, J. V.; Costantini, G.; Kern, K. Engineering atomic and molecular nanostructures at surfaces. *Nature* **2005**, *437*, 671−679.
(40) Bonifazi, D.; Mohnani, S.; Llanes-Pallas, A. Supramolecular Chemistry at Interfaces: Molecular Recognition on Nanopatterned Porous. *Chem. - Eur. J.* **2009**, *15*, 7004−7025.
(41) Goronzy, D. P.; Ebrahimi, M.; Rosei, F.; Arramel; Fang, Y.; De Feyter, S.; Tait, S. L.; Wang, C.; Beton, P. H.; Wee, A. T. S.; Weiss, P. S.; Perepichka, D. F. Supramolecular Assemblies on Surfaces: patterning, Functionality, and Reactivity. *ACS Nano* **2018**, *12*, 7445−7481.
(42) Grill, L.; Hecht, S. Covalent on-surface polymerization. *Nat. Chem.* **2020**, *12*, 115−130.
(43) Kumar, A.; Banerjee, K.; Liljeroth, P. Molecular assembly on two-dimensional materials. *Nanotechnology* **2017**, *28*, 082001.
(44) Auwärter, W. Hexagonal boron nitride monolayers on metal supports: Versatile templates for atoms, molecules and nanostructures. *Surf. Sci. Rep.* **2019**, *74*, 1−95.
(45) Ecija, D.; Urgel, J. I.; Seitsonen, A. P.; Auwärter, W.; Barth, J. V. Lanthanide-Directed Assembly of Interfacial Coordination Architectures-From Complex Networks to Functional Nanosystems. *Acc. Chem. Res.* **2018**, *51*, 365−375.
(46) Katoh, K.; Yoshida, Y.; Yamashita, M.; Miyasaka, H.; Breedlove, B. K.; Kajiwara, T.; Takaishi, S.; Ishikawa, N.; Isshiki, H.; Zhang, Y. F.; Komeda, T.; Yamagishi, M.; Takeya, J. Direct Observation of Lanthanide(III)-Phthalocyanine Molecules on Au(111) by Using Scanning Tunneling Microscopy and Scanning Tunneling Spectroscopy and Thin-Film Field-Effect Transistor Properties of Tb(III)- and Dy(III)-Phthalocyanine Molecules. *J. Am. Chem. Soc.* **2009**, *131*, 9967−9976.
(47) Vijayaraghavan, S.; Ecija, D.; Auwärter, W.; Joshi, S.; Seufert, K.; Seitsonen, A. P.; Tashiro, K.; Barth, J. V. Selective Supramolecular Fullerene-Porphyrin Interactions and Switching in Surface-Confined C60-Ce(TPP)2 Dyads. *Nano Lett.* **2012**, *12*, 4077−4083.
(48) Fahrendorf, S.; Atodiresei, N.; Besson, C.; Caciuc, V.; Matthes, F.; Blügel, S.; Kögerler, P.; Bürgler, D. E.; Schneider, C. M. Accessing 4f-states in single-molecule spintronics. *Nat. Commun.* **2013**, *4*, 2425.
(49) Cirera, B.; Matarrubia, J.; Kaposi, T.; Giménez-Agulló, N.; Paszkiewicz, M.; Klappenberger, F.; Otero, R.; Gallego, J. M.; Ballester, P.; Barth, J. V.; Miranda, R.; Galán-Mascarós, J. R.; Auwärter, W.; Ecija, D. Preservation of electronic properties of double-decker complexes on metallic supports. *Phys. Chem. Chem. Phys.* **2017**, *19*, 8282−8287.
(50) Zhang, Y.; Wang, Y.; Liao, P.; Wang, K.; Huang, Z.; Liu, J.; Chen, Q.; Jiang, J.; Wu, K. Detection and Manipulation of Charge States for Double-Decker DyPc2Molecules on Ultrathin CuO Films. *ACS Nano* **2018**, *12*, 2991−2997.
(51) Studniarek, M.; Wäckerlin, C.; Singha, A.; Baltic, R.; Diller, K.; Donati, F.; Rusponi, S.; Brune, H.; Lan, Y.; Klyatskaya, S.; Ruben, M.; Seitsonen, A. P.; Dreiser, J. Understanding the Superior Stability of Single-Molecule Magnets on an Oxide Film. *Adv. Sci.* **2019**, *6*, 1901736.
(52) Hellerstedt, J.; Cahlík, A.; Švec, M.; de la Torre, B.; Moro-Lagares, M.; Chutora, T.; Papoušková, B.; Zoppellaro, G.; Mutombo, P.; Ruben, M.; Zbořil, R.; Jelinek, P. On-surface structural and electronic properties of spontaneously formed Tb2Pc3 single molecule magnets. *Nanoscale* **2018**, *10*, 15553−15563.
(53) Katoh, K.; Komeda, T.; Yamashita, M. The Frontier of Molecular Spintronics Based on Multiple-Decker Phthalocyaninato TbIII Single-Molecule Magnets. *Chem. Rec* **2016**, *16*, 987−1016.
(54) Schwöbel, J.; Fu, Y.; Brede, J.; Dilullo, A.; Hoffmann, G.; Klyatskaya, S.; Ruben, M.; Wiesendanger, R. Real-space observation of spin-split molecular orbitals of adsorbed single-molecule magnets. *Nat. Commun.* **2012**, *3*, 953.
(55) Wäckerlin, C.; Donati, F.; Singha, A.; Baltic, R.; Rusponi, S.; Diller, K.; Patthey, F.; Pivetta, M.; Lan, Y.; Klyatskaya, S.; Ruben, M.; Brune, H.; Dreiser, J. Giant Hysteresis of Single-Molecule Magnets Adsorbed on a Nonmagnetic Insulator. *Adv. Mater.* **2016**, *28*, 5195−5199.
(56) Qi, Z. K.; Mishra, P.; Ara, F.; Oka, H.; Sainoo, Y.; Katoh, K.; Yamashita, M.; Komeda, T. Magnetic Hysteresis of Single-Molecule Magnets Adsorbed on Ferromagnetic Substrate. *ACS Nano* **2019**, DOI: 10.1021/acsnano.9b04428.
(57) Granet, J.; Sicot, M.; Kierren, B.; Lamare, S.; Chérioux, F.; Baudelet, F.; Fagot-Revurat, Y.; Moreau, L.; Malterre, D. Tuning the Kondo resonance in two-dimensional lattices of cerium molecular complexes. *Nanoscale* **2018**, *10*, 9123−9132.
(58) Ecija, D.; Auwärter, W.; Vijayaraghavan, S.; Seufert, K.; Bischoff, F.; Tashiro, K.; Barth, J. V. Assembly and manipulation of rotatable cerium porphyrinato sandwich complexes on a surface. *Angew. Chem., Int. Ed.* **2011**, *50*, 3872−3877.
(59) Urgel, J. I.; Ecija, D.; Vijayaraghavan, S.; Pörtner, M.; Bocquet, M.-L.; Auwärter, W.; Barth, J. V. In-Situ Growth of Gadolinium Phthalocyaninato Sandwich Complexes on the Ag(111) Surface. *ChemPhysChem* **2019**, *20*, 2301−2304.
(60) Diller, K.; Singha, A.; Pivetta, M.; Wäckerlin, C.; Hellwig, R.; Verdini, A.; Cossaro, A.; Floreano, L.; Velez-Fort, E.; Dreiser, J.; Rusponi, S.; Brune, H. Magnetic properties of on-surface synthesized single-ion molecular magnets. *RSC Adv.* **2019**, *9*, 34421−34429.
(61) Marbach, H. Surface-Mediated in Situ Metalation of Porphyrins at the Solid-Vacuum Interface. *Acc. Chem. Res.* **2015**, *48*, 2649−2658.
(62) Diller, K.; Papageorgiou, A. C.; Klappenberger, F.; Allegretti, F.; Barth, J. V.; Auwärter, W. In vacuo interfacial tetrapyrrole metallation. *Chem. Soc. Rev.* **2016**, *45*, 1629−1656.
(63) Schöniger, M.; Kachel, S. R.; Herritsch, J.; Schröder, P.; Hutter, M.; Gottfried, J. M. Direct synthesis of dilithium tetraphenylporphyrin: facile reaction of a free-base porphyrin with vapor-deposited lithium. *Chem. Commun.* **2019**, *55*, 13665−13668.
(64) Baklanov, A.; Garnica, M.; Robert, A.; Bocquet, M.-L.; Seufert, K.; Küchle, J. T.; Ryan, P. T. P.; Haag, F.; Kakavandi, R.; Allegretti, F.; Auwärter, W. On-Surface Synthesis of Nonmetal Porphyrins. *J. Am. Chem. Soc.* **2020**, *142*, 1871−1881.
(65) Hu, J.; Strand, F. S.; Chellappan, R. K.; Zhang, Z.; Shen, K.; Hu, J.; Ji, G.; Huai, P.; Huang, H.; Wang, P.; Li, Z.; Jiang, Z.; Wells, J. W.; Song, F. Direct Synthesis of Semimetal Phthalocyanines on a Surface with Insights into Interfacial Properties. *J. Phys. Chem. C* **2020**, *124*, 8247−8256.
(66) Bischoff, F.; Seufert, K.; Auwärter, W.; Seitsonen, A. P.; Heim, D.; Barth, J. V. Metalation of Porphyrins by Lanthanide Atoms at Interfaces: Direct Observation and Stimulation of Cerium Coordination to 2H-TPP/Ag(111). *J. Phys. Chem. C* **2018**, *122*, 5083−5092.
(67) Gottfried, J. M. Surface chemistry of porphyrins and phthalocyanines. *Surf. Sci. Rep.* **2015**, *70*, 259−379.
(68) Auwärter, W.; Ecija, D.; Klappenberger, F.; Barth, J. V. Porphyrins at interfaces. *Nat. Chem.* **2015**, *7*, 105−120.
(69) Dienel, T.; Gómez-Díaz, J.; Seitsonen, A. P.; Widmer, R.; Iannuzzi, M.; Radican, K.; Sachdev, H.; Müllen, K.; Hutter, J.; Gröning, O. Dehalogenation and Coupling of a Polycyclic Hydrocarbon on an Atomically Thin Insulator. *ACS Nano* **2014**, *8*, 6571−6579.
(70) Morchutt, C.; Björk, J.; Krotzky, S.; Gutzler, R.; Kern, K. Covalent coupling via dehalogenation on Ni(111) supported boron nitride and graphene. *Chem. Commun.* **2015**, *51*, 2440−2443.
(71) Urgel, J. I.; Schwarz, M.; Garnica, M.; Stassen, D.; Bonifazi, D.; Ecija, D.; Barth, J. V.; Auwärter, W. Controlling Coordination Reactions and Assembly on a Cu(111) Supported Boron Nitride Monolayer. *J. Am. Chem. Soc.* **2015**, *137*, 2420−2423.
(72) Zhao, W.; Dong, L.; Huang, C.; Win, Z. M.; Lin, N. Cu- and Pd-catalyzed Ullmann reaction on a hexagonal boron nitride layer. *Chem. Commun.* **2016**, *52*, 13225−13228.

(73) Rizzo, D. J.; et al. Revealing the Local Electronic Structure of a Single-Layer Covalent Organic Framework through Electronic Decoupling. *Nano Lett.* **2020**, *20*, 963−970.
(74) Riss, A.; Richter, M.; Pérez Paz, A.; Wang, X.-Y.; Raju, R.; He, Y.; Ducke, J.; Corral, E.; Wuttke, M.; Seufert, K.; et al. Polycyclic aromatic chains on metals and insulating layers by repetitive [3 + 2] cycloadditions. *Nat. Commun.* **2020**, *11*, 1490.
(75) Joshi, S.; Ecija, D.; Koitz, R.; Iannuzzi, M.; Seitsonen, A. P.; Hutter, J.; Sachdev, H.; Vijayaraghavan, S.; Bischoff, F.; Seufert, K.; Barth, J. V.; Auwärter, W. Boron Nitride on Cu(111): An Electronically Corrugated Monolayer. *Nano Lett.* **2012**, *12*, 5821−5828.
(76) Kottas, G. S.; Clarke, L. I.; Horinek, D.; Michl, J. Artificial Molecular Rotors. *Chem. Rev.* **2005**, *105*, 1281−1376.
(77) Shannon, R. D. Revised effective ionic radii and systematic studies of interatomic distances in halides and chalcogenides. *Acta Crystallogr., Sect. A: Cryst. Phys., Diffr., Theor. Gen. Crystallogr.* **1976**, *32*, 751−767.
(78) Gottfried, J. M.; Flechtner, K.; Kretschmann, A.; Lukasczyk, T.; Steinrück, H.-P. Direct Synthesis of a Metalloporphyrin Complex on a Surface. *J. Am. Chem. Soc.* **2006**, *128*, 5644−5645.
(79) Buchner, F.; Flechtner, K.; Bai, Y.; Zillner, E.; Kellner, I.; Steinrück, H.-P.; Marbach, H.; Gottfried, J. M. Coordination of Iron Atoms by Tetraphenylporphyrin Monolayers and Multilayers on Ag(111) and Formation of Iron-Tetraphenylporphyrin. *J. Phys. Chem. C* **2008**, *112*, 15458−15465.
(80) Di Santo, G.; Castellarin-Cudia, C.; Fanetti, M.; Taleatu, B.; Borghetti, P.; Sangaletti, L.; Floreano, L.; Magnano, E.; Bondino, F.; Goldoni, A. Conformational Adaptation and Electronic Structure of 2H-Tetraphenylporphyrin on Ag(111) during Fe Metalation. *J. Phys. Chem. C* **2011**, *115*, 4155−4162.
(81) Duncan, D. A.; Deimel, P. S.; Wiengarten, A.; Paszkiewicz, M.; Casado Aguilar, P.; Acres, R. G.; Klappenberger, F.; Auwärter, W.; Seitsonen, A. P.; Barth, J. V.; Allegretti, F. Bottom-Up Fabrication of a Metal-Supported Oxo-Metal Porphyrin. *J. Phys. Chem. C* **2019**, *123*, 31011−31025.
(82) Papageorgiou, A. C.; et al. Self-Terminating Protocol for an Interfacial Complexation Reaction in Vacuo by Metal-Organic Chemical Vapor Deposition. *ACS Nano* **2013**, *7*, 4520−4526.
(83) Fuggle, J. C.; Burr, A. F.; Watson, L. M.; Fabian, D. J.; Lang, W. X-ray photoelectron studies of thorium and uranium. *J. Phys. F: Met. Phys.* **1974**, *4*, 335−342.
(84) Cordero, B.; Gómez, V.; Platero-Prats, A. E.; Revés, M.; Echeverría, J.; Cremades, E.; Barragán, F.; Alvarez, S. Covalent radii revisited. *Dalton Trans.* **2008**, 2832−2838.
(85) Auwärter, W.; Seufert, K.; Bischoff, F.; Ecija, D.; Vijayaraghavan, S.; Joshi, S.; Klappenberger, F.; Samudrala, N.; Barth, J. V. A surface-anchored molecular four-level conductance switch based on single proton transfer. *Nat. Nanotechnol.* **2012**, *7*, 41.
(86) Auwärter, W.; Seufert, K.; Klappenberger, F.; Reichert, J.; Weber-Bargioni, A.; Verdini, A.; Cvetko, D.; Dell'Angela, M.; Floreano, L.; Cossaro, A.; Bavdek, G.; Morgante, A.; Seitsonen, A. P.; Barth, J. V. Site-specific electronic and geometric interface structure of Co-tetraphenyl-porphyrin layers on Ag(111). *Phys. Rev. B: Condens. Matter Mater. Phys.* **2010**, *81*, 245403.
(87) Komeda, T.; Isshiki, H.; Liu, J.; Zhang, Y.-F.; Lorente, N.; Katoh, K.; Breedlove, B. K.; Yamashita, M. Observation and electric current control of a local spin in a single-molecule magnet. *Nat. Commun.* **2011**, *2*, 217.
(88) Tanaka, H.; Ikeda, T.; Takeuchi, M.; Sada, K.; Shinkai, S.; Kawai, T. Molecular Rotation in Self-Assembled Multidecker Porphyrin Complexes. *ACS Nano* **2011**, *5*, 9575−9582.
(89) Ducke, J.; Riss, A.; Pérez Paz, A.; Seufert, K.; Schwarz, M.; Garnica, M.; Rubio, A.; Auwärter, W. Layered Insulator/Molecule/Metal Heterostructures with Molecular Functionality through Porphyrin Intercalation. *ACS Nano* **2018**, *12*, 2677−2684.
(90) Schulz, F.; Drost, R.; Hämäläinen, S. K.; Liljeroth, P. Templated Self-Assembly and Local Doping of Molecules on Epitaxial Hexagonal Boron Nitride. *ACS Nano* **2013**, *7*, 11121−11128.
(91) Liu, L.; Dienel, T.; Widmer, R.; Gröning, O. Interplay between Energy-Level Position and Charging Effect of Manganese Phthalocyanines on an Atomically Thin Insulator. *ACS Nano* **2015**, *9*, 10125−10132.
(92) Joshi, S.; Bischoff, F.; Koitz, R.; Ecija, D.; Seufert, K.; Seitsonen, A. P.; Hutter, J.; Diller, K.; Urgel, J. I.; Sachdev, H.; Barth, J. V.; Auwärter, W. Control of Molecular Organization and Energy Level Alignment by an Electronically patterned Boron Nitride Template. *ACS Nano* **2014**, *8*, 430−442.
(93) Herrera-Gomez, A.; Bravo-Sanchez, M.; Ceballos-Sanchez, O.; Vazquez-Lepe, M. O. Practical methods for background subtraction in photoemission spectra. *Surf. Interface Anal.* **2014**, *46*, 897−905.
(94) Romberg, R.; Frigo, S.; Ogurtsov, A.; Feulner, P.; Menzel, D. Photon stimulated desorption of neutral hydrogen atoms from condensed water and ammonia by resonant O1s and N1s excitation: search for the signature of ultrafast bond breaking. *Surf. Sci.* **2000**, *451*, 116−123.
(95) Nečas, D.; Klapetek, P. Gwyddion: an open-source software for SPM data analysis. *Cent. Eur. J. Phys.* **2012**, *10*, 181−188.
(96) Nuñez Beyerle, M. d. C. Thorium on a Silver(111)-Surface: Electronic Properties and Reactivity. M.Sc. thesis, Technical University of Munich, 2017.
(97) Blöchl, P. E. Projector augmented-wave method. *Phys. Rev. B: Condens. Matter Mater. Phys.* **1994**, *50*, 17953−17979.
(98) Perdew, J. P.; Burke, K.; Ernzerhof, M. Generalized Gradient Approximation Made Simple. *Phys. Rev. Lett.* **1996**, *77*, 3865−3868.
(99) Kresse, G.; Furthmüller, J. Efficient iterative schemes for ab initio total-energy calculations using a plane-wave basis set. *Phys. Rev. B: Condens. Matter Mater. Phys.* **1996**, *54*, 11169−11186.
(100) Grimme, S.; Antony, J.; Ehrlich, S.; Krieg, H. A consistent and accurate ab initio parametrization of density functional dispersion correction (DFT-D) for the 94 elements H-Pu. *J. Chem. Phys.* **2010**, *132*, 154104.
(101) Lorente, N.; Robles, R. STMpw. Zenodo: 2019; https://zenodo.org/record/3581159 (accessed Dec. 17, 2019); DOI: 10.5281/zenodo.3581159.

https://doi.org/10.1021/jacs.1c04982
J. Am. Chem. Soc. XXXX, XXX, XXX−XXX